

Interrelation between polycrystalline structure and time-dependent magnetic anisotropies in exchange-biased bilayers

Maximilian Merkel ^{*}, Rico Huhnstock, Meike Reginka , Dennis Holzinger, Michael Vogel, and Arno Ehresmann 

*Institute of Physics and Center for Interdisciplinary Nanostructure Science and Technology (CINaT), University of Kassel,
Heinrich-Plett-Strasse 40, 34132 Kassel, Germany*

Jonas Zehner and Karin Leistner

Leibniz IFW Dresden, Helmholtzstrasse 20, Dresden 01069, Germany



(Received 23 April 2020; revised 9 September 2020; accepted 23 September 2020; published 15 October 2020)

For polycrystalline exchange-biased thin films the macroscopic magnetic properties evolve from a complex interplay of different individual magnetic anisotropies which are directly connected to the grain volume distribution and to the crystal and interface structure of the layer system. A quantitative comparison of models describing a macroscopically observed exchange bias by the contributing anisotropies has in most cases been hampered by neglecting their time dependence with respect to data acquisition and storage times. Using a recently developed model we are able to connect time-dependent parts of the prevailing anisotropies with parameters describing the polycrystalline structure of the layer system. The model will be compared to experiments on a prototypical IrMn/CoFe bilayer, where structural and magnetic parameters have been systematically altered by varying the deposition rate of the antiferromagnetic layer and the field-cooling temperature. The combination of angular-resolved measurements obtained by vectorial magneto-optic Kerr magnetometry and a systematic analysis of the polycrystalline structure enables the disentanglement of the different anisotropy contributions to the macroscopic exchange bias and coercive fields and serves as a verification of the utilized model.

DOI: [10.1103/PhysRevB.102.144421](https://doi.org/10.1103/PhysRevB.102.144421)

I. INTRODUCTION

The exchange bias (EB) is a phenomenon occurring when an antiferromagnet (AF) and a ferromagnet (F) share a common interface, which hitherto has been observed not only in thin bilayer systems [1–4] and nanostructures based on the latter [5] but also in many other morphologies [5–9] besides systems composed of more complex magnetic materials [8]. In macroscopic hysteresis measurements, the effect manifests itself as a horizontal shift H_{EB} and a change in the coercive field H_C of the F hysteresis loop (Fig. 1), as compared to an unbiased F. These two macroscopic changes result from exchange interaction taking place at the interface between the adjacent layers, which in turn is influenced by different magnetic anisotropy contributions. The horizontal shift of the hysteresis loop H_{EB} determines the magnetic field compensating the field of opposite sign, which describes the pinning of the F due to exchange coupling to the AF. As the measurable quantity, the former will be designated by the term exchange-bias field H_{EB} following similar definitions in literature [10–13]. The exchange coupling occurs between interfacial magnetic moments of the F with fixed and rotatable moments of the AF, associated with a unidirectional (UDA) [1,2] and a rotatable (RMA) [10,11,14] magnetic anisotropy, respectively. For polycrystalline EB bilayers, the individual anisotropies and their interplay as well as the macroscopically

observable magnetic characteristics are directly connected to the AF [4,15,16] and F [17] grain volume distribution (GVD), the AF crystal structure [18,19], and the interface between the layers [3,4,20].

Recent investigations on domain engineering and patterning of polycrystalline EB thin films [21–27] reveal the necessity for a better understanding of the correlation between the granular microstructure, the magnetic anisotropies, and the macroscopic magnetic properties, being crucial in view of applications. For example, light-ion bombardment induced magnetic patterning of EB layer systems [21–24] with optimized magnetic stray field landscapes [28,29] can be utilized for the actuation of magnetic particles in lab-on-a-chip applications [30,31]. Since the impinging ions preferably influence smaller AF grains linked to the RMA [24], the desired minimization of the lateral size of artificial domains created by light-ion bombardment [23] depends on the tailoring of the different magnetic anisotropies via the microstructure.

In the last decades, a generalized description of the relation between the granular AF and the magnetic characteristics of polycrystalline EB thin films arose [4,10,11,16,21], increasing the understanding of the interaction between the AF and the F. The AF GVD is subdivided into classes of different thermal stability of their averaged uncompensated magnetic moment with respect to its parallel or antiparallel orientation relative to the F magnetization [4,21]. At a given temperature T , and a given duration of observation and sample storage, larger AF grains are thermally stable and pin the F magnetization causing a UDA and a corresponding EB shift H_{EB} . Smaller

^{*}max.merkel@physik.uni-kassel.de

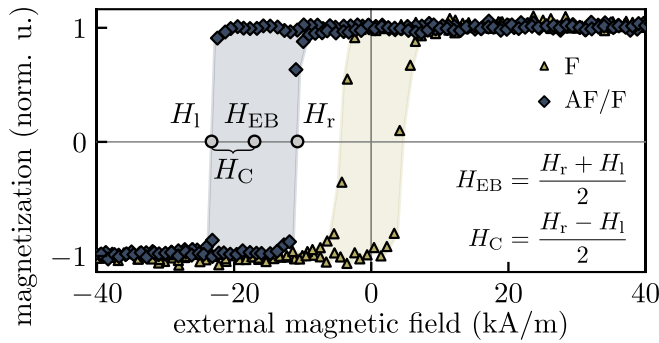


FIG. 1. Magnetization curve of an unbiased sample ($F \equiv \text{Cu}^{5\text{nm}}/\text{Co}_{70}\text{Fe}_{30}^{10\text{nm}}$) in comparison to an EB bilayer ($\text{AF}/F \equiv \text{Cu}^{5\text{nm}}/\text{Ir}_{17}\text{Mn}_{83}^{30\text{nm}}/\text{Co}_{70}\text{Fe}_{30}^{10\text{nm}}$) measured by longitudinal Kerr magnetometry with the sensitivity direction parallel to the easy axis. The horizontal shift H_{EB} and the coercivity H_{C} are determined from H_1 and H_r as the left and right zero crossings of the hysteresis loop, respectively.

grains are thermally unstable and might rotate their uncompensated interfacial magnetic moments after a certain time resulting in a RMA causing the increase of the coercive field H_{C} and the presence of coercivity along the magnetic hard axis [4,11]. A model proposed in Refs. [11,24] enables to disentangle the UDA, the RMA, and the F uniaxial magnetic anisotropy (FUMA) by comparing angular-resolved measurements of H_{EB} and H_{C} with numerical calculations based on an extended Stoner-Wohlfarth approach [32,33]. Retrieving the associated material constants allows to draw conclusions about the contributions of the different AF grain classes to the macroscopic magnetic characteristics [24].

Previously published models accounting for the RMA in polycrystalline EB systems often avoid actual time-dependent descriptions and represent limiting cases regarding the relaxation behavior of thermally unstable AF grains [11]. Either the direction of the RMA is parallel to the F magnetization in the case of AF grains with infinitesimally small relaxation times [34], or oriented along the direction of the probing external magnetic field for relaxation times larger than the duration of the magnetization reversal [14]. Coherent rotation approaches including a macroscopic AF uniaxial anisotropy to represent the time-dependent RMA cannot reproduce key features of the magnetization reversal, especially for external magnetic fields not aligned with the easy axis of the system [13,14], which is in contrast possible with models calculating the actual magnetic state of AF grains [16,35] demanding, however, higher complexity. The model proposed in Refs. [11,24] introduces a macroscopic RMA of unidirectional nature with an average relaxation time of thermally unstable AF grains controlling the time-dependent anisotropy direction related to the history of the F magnetization reversal. The model and method were developed and tested for a prototypical EB layer system in Ref. [11] and applied in Ref. [24] to quantify the effects of light-ion bombardment on the different grain classes. However, investigations with systematic variations of the AF GVD are still pending, which would serve as an experimental verification of the model and its applicability for determining microscopic parameters from macroscopic magnetization reversal measurements.

The GVD can in principle be tuned by additives [36], by seed layers [37], or by substrate temperature control during deposition [15,38–41]. The latter enables grain size control in sputter deposition, since the substrate temperature can be steered directly by a substrate heater or by varying the deposition rate either by changing the applied power or the gas pressure [38–40], keeping the microstructure of the residual system constant. For the present investigations, the AF GVD was systematically varied by changing the deposition rate of the AF layer via the applied power. The variation of deposition parameters gives rise to a rich phase diagram regarding the microstructural properties of the deposited thin films where not only the grain size, but also the crystal structure, the surface and interface structure, as well as the growth morphology, is affected [38–40,42]. In view of AF grain size control via the deposition rate [15,41], the disentanglement of the structural properties in correlation with the magnetic characteristics of polycrystalline exchange-bias systems is crucial [3,4,19].

The surface topography of the granular AF is characterized by atomic force microscopy (AFM) in order to extract the distribution of contact interfaces, while the crystal structure is analyzed by x-ray diffraction (XRD). The magnetic properties, H_{EB} and H_{C} , are determined from angular-resolved magnetization reversal curves utilizing the magneto-optic Kerr effect (MOKE). Finally, the correlation of the structural and the magnetic characteristics enables the disentanglement of the FUMA, the UDA, and the RMA for controlled GVD, distinguishing between thermally unstable and thermally stable parts of the polycrystalline AF for measurements at room temperature. This evidences the applicability, reproducibility, and versatility of the developed model describing polycrystalline EB systems.

II. EXPERIMENT

A. Sample preparation

Two different types of layer systems were deposited on naturally oxidized Si(100) using rf-sputter deposition with an applied in-plane magnetic field set to 28 kA/m. The base pressure was $<10^{-6}$ mbar and the working pressure $\approx 1 \times 10^{-2}$ mbar. Layer system type A ($\text{Cu}^{5\text{nm}}/\text{Ir}_{17}\text{Mn}_{83}^{30\text{nm}}/\text{Co}_{70}\text{Fe}_{30}^{10\text{nm}}/\text{Si}^{20\text{nm}}$) was chosen to consist of a 5 nm Cu seed layer in order to induce a (111) crystal orientation in the 30 nm $\text{Ir}_{17}\text{Mn}_{83}$ AF layer [18]. On top of that, a 10 nm $\text{Co}_{70}\text{Fe}_{30}$ layer was deposited because of its relatively high magnetocrystalline anisotropy and critical temperature [4,43,44]. The 20 nm Si capping layer protects the underlying system from oxidation and enhances the contrast in the magneto-optical measurements [11]. For layer system type B ($\text{Cu}^{5\text{nm}}/\text{Ir}_{17}\text{Mn}_{83}^{30\text{nm}}$), the F and the capping layer were omitted to determine the AF grain interface distribution (GID) of the polycrystalline $\text{Ir}_{17}\text{Mn}_{83}$ layer via AFM. The GID represents the distribution of contact interfaces directly connected with the GVD in the case of a columnar grain growth. For tuning the GVD of the polycrystalline AF layer the $\text{Ir}_{17}\text{Mn}_{83}$ deposition rate η_{AF} was varied via the dc bias voltage U_{AF} set between 300 and 800 V with an increment of 50 V (Table I), where an increase of the mean grain sizes is expected for increasing η_{AF} [15,41], due to the scaling of the substrate temperature during the deposition [38–40,42]. The

TABLE I. Deposition rates $\eta_{AF}^{A/B}$ of the AF layer in dependence of the dc bias voltage U_{AF} for layer systems A and B (see Sec. II A) and the mean grain radius $\langle r_{AF} \rangle$ and the square root of the variance $\sqrt{\sigma_{r_{AF}}}$ determined from measured AF GID of layer systems B (see Sec. IV A).

U_{AF} (V)	η_{AF}^A ($\frac{\text{nm}}{\text{min}}$)	η_{AF}^B ($\frac{\text{nm}}{\text{min}}$)	$\langle r_{AF} \rangle$ (nm)	$\sqrt{\sigma_{r_{AF}}}$ (nm)
300	0.87 ± 0.02	0.94 ± 0.04	7.6 ± 1.5	3.4 ± 1.8
350	1.24 ± 0.02	1.27 ± 0.02	6.7 ± 1.1	3.3 ± 0.9
400	1.64 ± 0.06	1.75 ± 0.11	6.8 ± 1.3	3.6 ± 1.2
450	1.91 ± 0.09	2.26 ± 0.08	5.7 ± 0.9	2.3 ± 0.7
500	2.46 ± 0.08	2.47 ± 0.15	7.1 ± 1.4	3.6 ± 1.4
550	2.79 ± 0.14	3.20 ± 0.15	6.8 ± 1.4	3.4 ± 1.6
600	3.52 ± 0.08	3.72 ± 0.25	4.2 ± 0.5	1.6 ± 0.5
650	4.00 ± 0.11	4.75 ± 0.17	5.0 ± 0.7	2.0 ± 0.4
700	4.87 ± 0.15	5.16 ± 0.12	7.1 ± 1.5	3.8 ± 1.5
750	5.47 ± 0.10	5.93 ± 0.11	9.7 ± 2.1	6.3 ± 1.6
800	6.06 ± 0.14	7.09 ± 0.32	13.3 ± 2.1	5.5 ± 2.0

Cu buffer layer below the $\text{Ir}_{17}\text{Mn}_{83}$ layer was deposited using a dc bias voltage set to $U_{Cu} = 600$ V for which the deposition rates were determined to be $\eta_{Cu}^A = (5.99 \pm 0.22)$ nm/min and $\eta_{Cu}^B = (6.40 \pm 0.19)$ nm/min, with respect to layer systems of types A and B. The CoFe layer and the Si capping layer were deposited using $U_{CoFe} = 600$ V and $U_{Si} = 700$ V, respectively, with $\eta_{CoFe}^A = (3.00 \pm 0.06)$ nm/min and $\eta_{Si}^A = (3.45 \pm 0.28)$ nm/min. The rates were determined from the height profile and the corresponding deposition time of a calibration layer deposited on a substrate masked prior to the deposition. The desired nominal layer thicknesses were ensured by choosing deposition times according to the rates. Furthermore, the $\text{Ir}_{17}\text{Mn}_{83}$ and the $\text{Co}_{70}\text{Fe}_{30}$ layers were deposited utilizing alloy targets with the same composition.

Type A layer systems were field cooled in an external in-plane magnetic field set to 64 kA/m at temperatures between $T_{FC} = 423.15$ and 623.15 K in steps of 50 K for 60 min and magnetically characterized after 24 h.

B. Structural and magnetic characterization

The AF GID for layer systems of type B was determined by AFM in contact mode directly after the deposition measuring several spots on the surface with a nominal resolution of 0.49 nm/pixel. The surface structure was analyzed utilizing the Watershed algorithm provided by the evaluation software for scanning probe microscopy, GWYDDION (V.2.49) [45]. For noise reduction, the raw data were convolved with a two-dimensional Gaussian with a full width at half maximum ΔG and subsequently treated with a maximum filter emphasizing the grain boundaries using a disk diameter ΔD . The two postprocessing parameters were set to $\Delta G = \Delta D = 2.5$ nm, setting the lower bound for the GID analysis.

An x-ray diffractometer in Bragg-Brentano geometry ($\vartheta/2\vartheta$ scan) was utilized to characterize the crystal structure of layer systems of type A for $T_{FC} = 623.15$ K with an in-plane sample rotation of 0.5 Hz using the Co $K\alpha_1$ line with $\lambda_{CoK\alpha_1} = 0.1789$ nm. An angle range between $2\vartheta = 40^\circ$ and 60° was chosen with an increment of $\Delta 2\vartheta = 0.01^\circ$ and a measurement time of 10 s per angle step. Lorentzian profiles $\mathcal{L}(2\vartheta, \vartheta_0, s, \Delta_{2\vartheta})$ with the integrated peak area s , the full

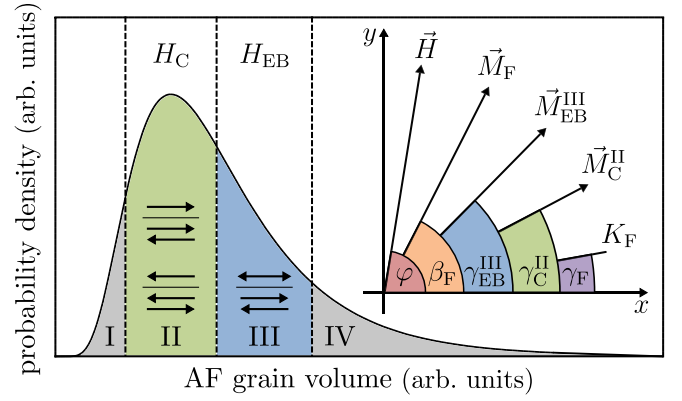


FIG. 2. Schematic distribution of AF grain volumes divided into four classes depending on their thermal stability for a given temperature, measurement, and storage time. Inset: Angles corresponding to the relevant vectors used in the presented model with respect to an arbitrary reference frame. \vec{H} is the external magnetic field with its azimuthal angle φ . \vec{M}_F is the F magnetization vector with the angle β_F . K_F is the energy density of the FUMA with its easy direction defined by γ_F . \vec{M}_C^{II} and \vec{M}_C^{III} are the superposed interface magnetic moments related to AF grains of classes II and III with γ_C^{II} and γ_C^{III} as the corresponding azimuthal angles, respectively. Arrows schematically depict AF magnetic moments (\rightleftharpoons) influenced by the reversal of the F magnetization (\rightarrow and \leftarrow).

width at half maximum $\Delta_{2\vartheta}$, and the peak position ϑ_0 were fitted to the identified diffraction peaks. Scans for layer systems without field cooling showed no significant deviation from the measured scans for $T_{FC} = 623.15$ K and are not discussed.

Samples of type A were magnetically characterized by angular-resolved vectorial MOKE magnetometry with a setup described in Ref. [11]. Angular-resolved magnetization curves determining the magnetization component parallel to the applied external field were obtained for angles between $\varphi = 0^\circ$ and 450° with a resolution of 1° and a hysteresis duration of $t_{hys} = (76 \pm 1)$ s, which has been kept constant throughout all measurements. The magnetization curves obtained for angles between $\varphi = 360^\circ$ and 450° were used to exclude large training effects.

III. POLYCRYSTALLINE MODEL

For numerical calculations of magnetization curves of polycrystalline EB systems and the interpretation of the obtained experimental results, the model in Ref. [11] was utilized and its main characteristics are summarized here. The polycrystalline model represents an extended Stoner-Wohlfarth approach [32,33], where a coherent rotation of an in-plane F magnetization during a magnetization reversal process is assumed. Based on the free energy of the F layer, $E(\beta_F)$, in dependence of its azimuthal angle β_F with respect to an arbitrary reference frame (see inset of Fig. 2 for angle definitions), β_F is calculated for varying external field strength H via minimizing the energy interface density $E(\beta_F)/A$ with respect to the interface A using the perfect delay convention [11,46].

The free energy is a sum of the F potential energy in the external magnetic field and several magnetic anisotropy

terms. The intrinsic anisotropy of the F layer of thickness t_F and saturation magnetization M_S is assumed to be uniaxial (FUMA) with an energy density K_F and an azimuthal angle γ_F , since the uniaxial anisotropy induced during the deposition in an external magnetic field outweighs the natural biaxial magnetocrystalline anisotropy of CoFe [11]. The granular AF is modeled by dividing its GVD into four classes of different thermal stability (Fig. 2) [4,11]. Each AF grain i possesses an energy barrier ΔE_i between a global and a local minimum for the grain-averaged uncompensated interface magnetic moment relative to the F magnetization direction [21,47]. In first order, the energy barriers can be expressed by the product $\Delta E_i = K_{AF,i} V_{AF,i}$ of the anisotropy $K_{AF,i}$ of the individual grain and its volume $V_{AF,i}$ allowing to connect the GVD and the distribution of relaxation times

$$\tau_i = \tau_0 \exp \left\{ \frac{\Delta E_i}{k_B T} \right\} \quad (1)$$

between local and global energy minima. $\nu_0 = 1/\tau_0$ represents the characteristic frequency for spin reversal of the AF grains [48], T the temperature, and k_B Boltzmann's constant. The distribution of relaxation times among the grains is subdivided into four different classes with different thermal stability with respect to measurement and storage temperatures and times. Small AF grains are thermally unstable and are either superparamagnetic (class I) or have relaxation times in the order of the hysteresis duration t_{Hys} (class II) and consequently contribute to the F coercivity H_C . The anisotropy generated by class II grains is a RMA, since the averaged magnetic moment of those grains can rotate during the magnetization reversal (Fig. 2) and continuously relax into a state parallel to the steadily changing F magnetization, which consequently needs to overcome an additional torque [11,14,16]. Larger grains of classes III and IV are thermally stable and have relaxation times longer than t_{Hys} . While grains of class III contribute to H_{EB} with a specific direction of the UDA, which is set during field cooling at elevated temperatures or during deposition in an external magnetic field, the UDA of class IV grains cannot be aligned by field cooling and remain randomly distributed due their high energy barriers [4,11]. It is important to point out that the connection of the distribution of relaxation times with the GVD is only valid for a constant K_{AF} , which might not be valid especially for small grains [49]. For small V_{AF} the decrease in volume is accompanied by a reduction of K_{AF} , which in this study is assumed to be only relevant for superparamagnetic grains populating class I.

The energy terms connected to the grains of classes II and III are modeled in a way that the F magnetization interacts via exchange interaction with the AF magnetization of the particular grain class,

$$\vec{M}_{C/EB}^{II/III} = \sum_i \vec{m}_{AF,i}^{II/III}, \quad (2)$$

caused by the vector sum of the individual grain-averaged uncompensated magnetic AF moments $\vec{m}_{AF,i}^{II/III}$. Furthermore, the thermally unstable grains of class II are described with an average relaxation time τ_C^{II} and the angle of the time-dependent rotatable anisotropy axis with the corresponding angle $\gamma_C^{II}(t) = \beta_F(t - \tau_C^{II})$. For each step in the calculation of the F hysteresis, for which $\beta_F(t)$ needs to be determined,

$\gamma_C^{II}(t)$ is derived from the history of the F magnetization at the time point $t - \tau_C^{II}$. J_C^{II} and J_{EB}^{III} are defined as the energy area densities of the RMA and UDA. They are directly correlated to the number of grains in the respective class contributing either to H_C or H_{EB} , respectively [4,11]. The free energy interface density of the F layer consequently consists of the potential energy of the F magnetization in an external magnetic field, the energy density of the FUMA, and the energy densities regarding the described RMA and UDA,

$$\begin{aligned} \frac{E(\beta_F)}{A} = & -\mu_0 H M_S t_F \cos(\beta_F - \varphi) \\ & + K_F t_F \sin^2(\beta_F - \gamma_F) \\ & - J_C^{II} \cos(\beta_F - \gamma_C^{II}(t)) \\ & - J_{EB}^{III} \cos(\beta_F - \gamma_{EB}^{III}), \end{aligned} \quad (3)$$

where μ_0 is the magnetic permeability in vacuum [11].

To compare the model with the experimentally obtained angular-resolved functions $H_{EB}(\varphi)$ and $H_C(\varphi)$, magnetization curves $M_F(H)$ are simulated for varying angle φ of the external magnetic field. The EB shift and the coercivity are directly derived from the zero crossings of the hysteresis loops as sketched in Fig. 1.

IV. RESULTS AND DISCUSSION

A. Structural properties

Surface topography. In Fig. 3(a) the polycrystalline structure of the IrMn layer is exemplarily shown for $\eta_{AF} = 4.75$ and 5.93 nm/min, showing that for higher η_{AF} there is a larger mean grain contact interface.

With the given spatial resolution $\kappa = 0.49$ nm/pixel and the determined number of pixels A_G^* (pixel²) for an identified grain, an equivalent grain interface $A_G = A_G^* \kappa^2 = \pi r_G^2$ (nm²) with the equivalent grain radius r_G can be calculated. For columnar grains, r_G is equal to the cross-section radius of the respective grain. However, if the growth behavior is not columnar, it is not possible to conclude from the visible GID on the GVD. Assigning to each identified grain an equivalent grain radius, a histogram can be derived representing the probability density $\varrho(r_G)$ for the occurrence of grains with a certain radius r_G following a lognormal distribution with the parameters μ and s [4,15,41]:

$$\varrho(r_G, \mu, s) = \frac{1}{\sqrt{2\pi} s r_G} \exp \left\{ -\frac{(\ln\{r_G\} - \mu)^2}{2s^2} \right\}. \quad (4)$$

Histograms displaying the proportion of identified AF grains as a function of the equivalent grain radius r_{AF} in bins of 2.5 nm width of the IrMn layer for deposition rates $\eta_{AF} \geq 3.72$ nm/min are shown in Fig. 3(b) with corresponding fit curves $\varrho(r_{AF}, \mu, s)$. The mean grain radii are depicted with dashed lines and connected to the related data points in Fig. 3(c), where the mean grain radius $\langle r_{AF} \rangle$ and the square root of the variance $\sqrt{\sigma_{r_{AF}}}$ are presented in dependence of η_{AF} . It can be observed that $\langle r_{AF} \rangle$ increases between $\langle r_{AF} \rangle = (4.1 \pm 0.5)$ nm and (13 ± 2) nm from the threshold $\eta_{AF} = 3.72$ nm/min, which is accompanied by an increase of $\sqrt{\sigma_{r_{AF}}}$ with a maximum at $\eta_{AF} = 5.93$ nm/min. Consequently, not only $\langle r_{AF} \rangle$ is shifted towards larger radii for increasing

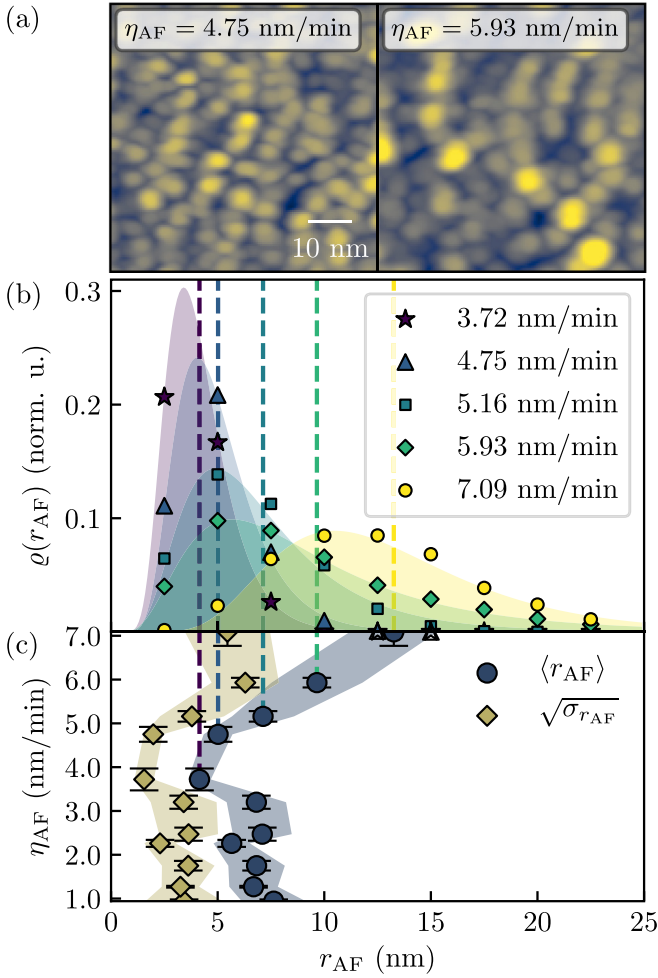


FIG. 3. (a) Surface topography of the IrMn layer for $\eta_{AF} = 4.75$ nm/min and 5.93 nm/min. (b) Distributions $\rho(r_{AF})$ of the grain radius r_{AF} for increasing deposition rates $\eta_{AF} \geq 3.72$ nm/min. Shaded curves are corresponding fits with a lognormal distribution. (c) The mean grain radius $\langle r_{AF} \rangle$ and the square root of the variance $\sqrt{\sigma_{r_{AF}}}$ are extracted, where the mean grain radii (dashed lines) in correspondence to the curves, depicted in (b), are connected. The shaded areas represent the error margins of $\langle r_{AF} \rangle$ and $\sqrt{\sigma_{r_{AF}}}$.

η_{AF} but also the broadness of the distribution is enhanced. For $\eta_{AF} < 3.72$ nm/min, $\langle r_{AF} \rangle$ and $\sqrt{\sigma_{r_{AF}}}$ are constant with $\langle r_{AF} \rangle = (6.8 \pm 1.7)$ nm on average.

The extracted root-mean-square surface roughness showed no trend on η_{AF} . Therefore, only the GID of the IrMn layer scales with η_{AF} , without significantly affecting the surface roughness.

Crystal structure. $\vartheta/2\vartheta$ scans are presented in Fig. 4(a), showing the $\text{Ir}_{17}\text{Mn}_{83}$ (111) and $\text{Co}_{70}\text{Fe}_{30}$ (110) crystal orientation [50]. For the present deposition parameters and compositions, $\text{Ir}_{17}\text{Mn}_{83}$ and $\text{Co}_{70}\text{Fe}_{30}$ are expected to show a face-centered-cubic (fcc) and body-centered-cubic (bcc) crystallographic phase, respectively, where it is assumed that the atoms do not have a specific lattice-site preference [19,51]. The IrMn (111) orientation, correlated with a large magnetocrystalline anisotropy of the AF grains and a large areal density of interfacial magnetic moments [18], is most prominent for $\eta_{AF} \geq 4.0$ nm/min and least shifted from the

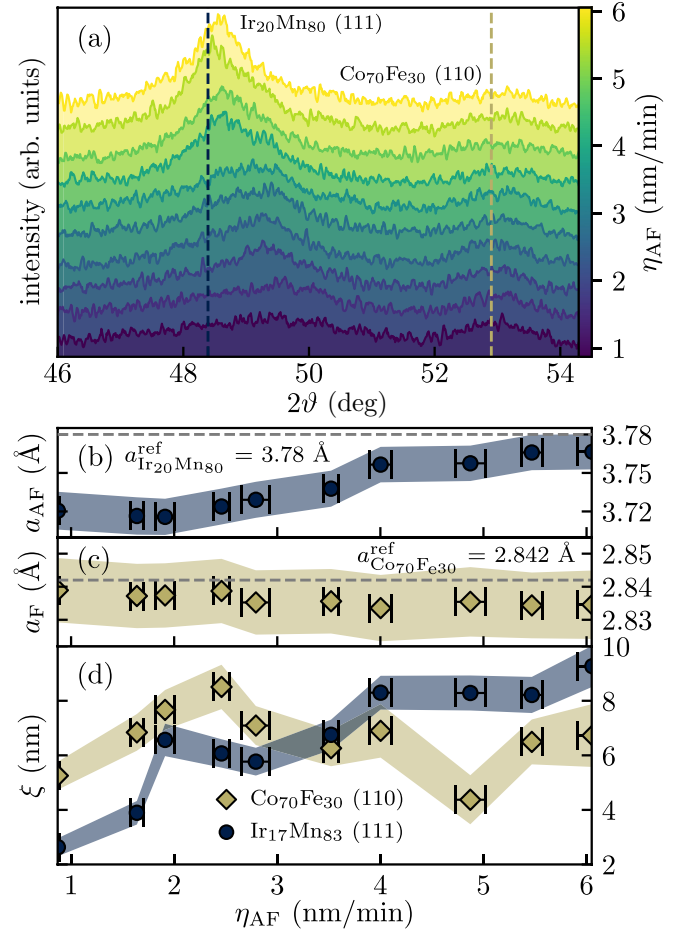


FIG. 4. (a) $\vartheta/2\vartheta$ scans for increasing η_{AF} with peak positions of the $\text{Ir}_{20}\text{Mn}_{80}$ (111) and the $\text{Co}_{70}\text{Fe}_{30}$ (110) crystal orientation [50]. The lattice parameters (b) a_{AF} and (c) a_F and the coherence length (d) ξ of the $\text{Ir}_{17}\text{Mn}_{83}$ and the $\text{Co}_{70}\text{Fe}_{30}$ layers are presented in dependence on η_{AF} . Reference values $a_{\text{Ir}_{20}\text{Mn}_{80}}^{\text{ref}}$ and $a_{\text{Co}_{70}\text{Fe}_{30}}^{\text{ref}}$ are added for comparison [50].

$\text{Ir}_{20}\text{Mn}_{80}$ reference peak [50], while for lower η_{AF} a peak broadening and a significant peak shift is observable. The peak with respect to the CoFe (110) orientation appears to be independent on η_{AF} .

From the peak positions $2\vartheta_{(111)}$ and $2\vartheta_{(110)}$, the lattice parameters $a_{AF} = \sqrt{3}\lambda_{\text{CoK}\alpha_1}/2 \sin \vartheta_{(111)}$ and $a_F = \sqrt{2}\lambda_{\text{CoK}\alpha_1}/2 \sin \vartheta_{(110)}$ can be determined [Figs. 4(b) and 4(c)] [52,53]. Whereas a_{AF} with respect to the IrMn layer increases for increasing η_{AF} and approaches $a_{AF} = 3.762 \pm 0.014$ Å for $\eta_{AF} \geq 4$ nm/min, lying slightly below the reference value $a_{\text{Ir}_{20}\text{Mn}_{80}}^{\text{ref}} = 3.78$ Å, the lattice parameter a_F of the CoFe layer equals $a_{\text{Co}_{70}\text{Fe}_{30}}^{\text{ref}} = 2.842$ Å within its error margin [50].

The coherence length ξ , representing a lower bound of the crystallite height, is connected with the full width at half maximum $\Delta_{2\vartheta}$ via the Scherrer equation $\xi = K_S \lambda_{\text{CoK}\alpha_1} / \Delta_{2\vartheta} \cos \vartheta$ [52,53]. K_S is the Scherrer factor which is defined by the geometry and the crystal orientation of the investigated crystallites [53]. A detailed analysis regarding cylindrical crystallites assuming columnar growth is given in Ref. [54] enabling the estimation of K_S depending on the diffraction angle of the respective peak, the nominal layer

thickness, and the mean grain radius [Fig. 3(c)]. ξ is presented in Fig. 4(d) for the IrMn and the CoFe layers as ξ_{AF} and ξ_F , respectively, where ξ_F shows no clear dependence on η_{AF} within the uncertainty margin and equals $\langle \xi_F \rangle = (6.6 \pm 1.8)$ nm on average. Contrarily, regarding the IrMn layer, an increase between $\xi_{AF} = 2.6$ and 8.3 nm occurs for $\eta_{AF} \leq 4.0$ nm/min. A plateau of $\xi_{AF} = (8.5 \pm 1.2)$ nm is reached for larger η_{AF} , indicating that the crystallite height, which contributes to the peak broadening, remains constant [52,53]. Since instrumental contributions to the peak broadening should have an equal effect on all measured diffractograms, the peak broadening for $\eta_{AF} < 4.0$ nm/min is expected to arise from interrupted grain growth, as well as inhomogeneities due to lattice defects, concentration gradients, and local stoichiometric variations. This results in inhomogeneous strain of the crystal lattice consequently introducing a significant peak broadening of the diffraction peaks [39,40,42,53].

Polycrystalline microstructure. Comparing the crystal structure (Fig. 4) with the GID determined from the IrMn surface topography (Fig. 3), two phases regarding the polycrystalline microstructure of IrMn can be clearly distinguished for $\eta_{AF} < 3.52$ and $\eta_{AF} \geq 4$ nm/min, whereas the crystal structure of CoFe appears to be unaffected. For decreasing η_{AF} an inhomogeneous crystal structure of the IrMn layer is observed, whereas for increasing η_{AF} , the AF GID can be scaled with an apparently independent crystal structure and pronounced (111) crystal orientation. Additionally, the coherence length, as the lower bound for the crystallite height, stays constant for large η_{AF} , indicating that, whereas the AF GID is scaled with η_{AF} , the average AF grain height is unaltered. Consequently, columnar grain growth with a homogenous crystal structure is expected for increasing η_{AF} with a η_{AF} -tunable GVD, which is consistent with common structure zone models [38–40,42].

B. Magnetic properties

Easy-axis analysis. The dependence on T_{FC} of the exchange-bias field H_{EB} and the coercivity H_C for increasing η_{AF} is depicted in Fig. 5 obtained from MOKE measurements with the sensitivity direction parallel to the easy axis of the layer systems.

For $\eta_{AF} \geq 3.52$ nm/min, a significant increase of the absolute value $|H_{EB}|$ of the exchange-bias field H_{EB} and the coercivity H_C can be observed, where the slope of H_C is not significantly changed for larger T_{FC} . In contrast, an η_{AF} -dependent enhancement of $|H_{EB}|$ can be observed for increasing T_{FC} , with the highest relative increase at $\eta_{AF} = 5.47$ nm/min for $T_{AF} \geq 573.15$ K.

Both trends can be correlated to the scaling of the AF GID for increasing η_{AF} and the IrMn crystal structure for $\eta_{AF} \geq 4.0$ nm/min as presented in Sec. IV A. This is in agreement with the polycrystalline model [11], similar investigations [15,41,48,55], and common structure zone models [38–40,42], where in general a larger grain size is expected for increasing deposition rate in sputter-deposited polycrystalline thin films. Consequently, assuming a monotonous relation between the scaling of the GVD and the analyzed GID, the enhancement of $|H_{EB}|$ and H_C for increasing η_{AF} results from larger mean grain sizes and a broadening of the GVD. For

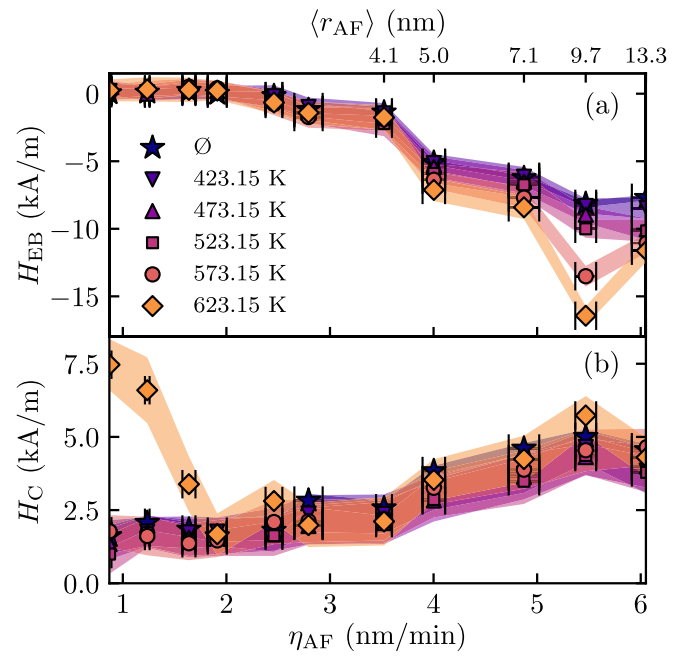


FIG. 5. (a) H_{EB} and (b) H_C for increasing η_{AF} and T_{FC} between 423.15 and 623.15 K as well as for the untreated case \emptyset . The upper abscissa shows the determined mean grain radii $\langle r_{AF} \rangle$ of the GID corresponding to η_{AF} .

increasing η_{AF} , therefore, not only more AF grains can be attributed to class III, mediating H_{EB} , but also the amount of grains assigned to class II, mediating H_C , increases, since the grain class boundaries are expected to be constant for fixed measurement and storage conditions. In the case of no field cooling, the relative enhancement of $|H_{EB}(\eta_{AF})|$ and $H_C(\eta_{AF})$ seems to decrease for large η_{AF} and turns into a relative reduction for $\eta_{AF} \geq 6.06$ nm/min, since the number of grains below a certain class boundary is not high enough to cause a further increase in the number of grains belonging to the adjacent class for increasing η_{AF} . Furthermore, if the GVD is altered, grains are not only transferred from classes I and II to classes II and III, respectively, but also from class III to class IV. Those grains cannot be aligned and do not contribute to H_{EB} .

Whereas grains of class II are not affected by field cooling, the uncompensated moments of class III grains are aligned to form the macroscopically observed H_{EB} . If T_{FC} is increased, the number of grains contributing to H_{EB} increases, which can be seen in Fig. 5(a). The comparably high variance of the GID for $\eta_{AF} = 5.93$ nm/min in Fig. 3(c) is therefore the prerequisite for the largest relative enhancement of $|H_{EB}|$ for increasing T_{FC} at approximately the same η_{AF} , since the corresponding GVD is more susceptible to the shift of the boundary between the grains of classes III and IV induced by the field cooling. $\eta_{AF} < 3.52$ nm/min result in no significant exchange-bias field and for $T_{FC} \leq 573.15$ K in a constant value for the coercivity $H_C = (1.6 \pm 0.8)$ kA/m, because the average grain volume and the variance of the GVD are too small for a sufficient number of grains contributing to H_{EB} .

Surprisingly, in the case of $T_{FC} = 623.15$ K for $\eta_{AF} \leq 1.64$ nm/min, a significant increase of H_C is observable for

decreasing η_{AF} , presumably due to a melting point depression for small grain sizes [56,57]. For small η_{AF} a larger number of small grains is present possibly possessing a relatively high percentage of defects and inhomogeneities, motivating the hypothesis that at $T_{FC} = 623.15$ K those grains which are superparamagnetic (class I) melt together forming larger grains and that defects are annealed affecting the grains' anisotropy, which might result in a transfer of the AF grains from class I to class II. Since it is assumed that $\text{Ir}_{17}\text{Mn}_{83}$ has an unordered chemical phase [19], the melting temperature $T_m^{\text{Ir}_{17}\text{Mn}_{83}}$ of the mixed crystals can be estimated by the average composition and the melting temperatures $T_m^{\text{Ir}} \approx 2739$ K and $T_m^{\text{Mn}} \approx 1519$ K [58,59] to $T_m^{\text{Ir}_{17}\text{Mn}_{83}} \approx 1726$ K [58]. Therefore a melting point depression to $T_{FC}/T_m^{\text{Ir}_{17}\text{Mn}_{83}} \approx 36\%$ can be deduced from the present data. This is in accordance with available literature data [56,57,60,61].

Azimuthal dependence and model calculations. Since the orientation φ of the external magnetic field is crucial for detecting the directions of easy and hard axes lying in the plane of a magnetic thin film, angular-resolved measurements were performed with layer systems after a field-cooling procedure at $T_{FC} = 623.15$ K. $\varphi = 0^\circ$ corresponds to the direction of the external magnetic field during deposition and the field during the field-cooling procedure and is collinear to the induced FUMA and UDA. $H_{EB}(\varphi)$ and $H_C(\varphi)$ are compared to simulated dependencies $H_{EB}^{\text{sim}}(\varphi)$ and $H_C^{\text{sim}}(\varphi)$ retrieved from an extended Stoner-Wohlfarth model based on Eq. (3). Small deviations from the mirror symmetry of $H_{EB}(\varphi)$ and $H_C(\varphi)$ in the vicinity of the easy axis can be attributed to a misalignment $|\gamma_F - \gamma_{EB}| \leq 2^\circ$ between the FUMA and the UDA [11,24,62,63]. However, in order to minimize the number of relevant model parameters, the angles of the FUMA and UDA are set to $\gamma_F = \gamma_{EB}^{\text{III}} = 0^\circ$ defining the easy axis, because of the strong intrinsic anisotropy of the utilized F [11,64]. Additionally, a constant orientation of the samples in different steps during preparation and characterization could experimentally be guaranteed utilizing a mechanical stop ensuring that the impact of noncollinear field cooling [62] is negligible. For the chosen thickness of $t_F = 10$ nm, the saturation magnetization was taken from literature as $M_S = 1230$ kA/m [65]. The residual set of fit parameters $x = \{K_F, \tau_C^{\text{II}}, J_C^{\text{II}}, J_{EB}^{\text{III}}\}$ consists of the energy density K_F of the FUMA, the average relaxation time τ_C^{II} of AF grains of class II, the energy density J_C^{II} of coercivity mediating grains of class II as well as the energy density J_{EB}^{III} of EB field mediating grains of class III. An explanation on how the fitting of the model calculations to the experimental data was achieved and how the uncertainties were estimated can be found in the Appendix.

Measured curves $H_{EB}(\varphi)$ and $H_C(\varphi)$ as well as corresponding model calculations for the respective optimal set of parameters are exemplarily depicted in Figs. 6(a), 6(b), and 6(c) for deposition rates $\eta_{AF} = 0.87, 2.46$, and 5.47 nm/min, respectively. While in Fig. 6(c) a commonly observed angular-resolved measurement of H_{EB} and H_C is visible with the prominent $-\cos(\varphi)$ behavior for the exchange-bias shift and sharp peaks regarding the coercivity along the easy axis of the system [11,13,24], the measurements look rather different for Figs. 6(a) and 6(b) representing deposition rates $\eta_{AF} < 3.52$ nm/min. It is visible that for decreasing η_{AF} the coercivity peaks widen from the easy axis and develop satellite

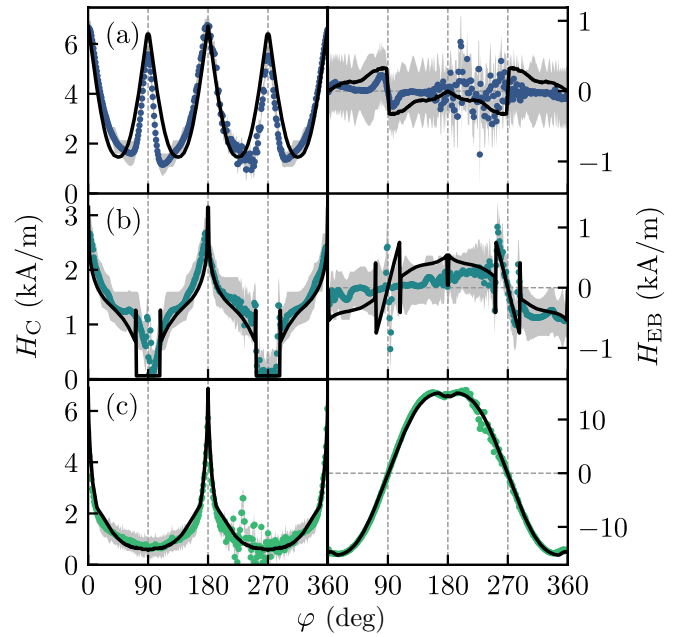


FIG. 6. $H_C(\varphi)$ (left column) and $H_{EB}(\varphi)$ (right column) for (a) $\eta_{AF} = 0.87$ nm/min, (b) $\eta_{AF} = 2.46$ nm/min, and (c) $\eta_{AF} = 5.47$ nm/min, where the black solid lines correspond to model calculations.

peaks near the hard axis [Fig. 6(b)] which merge together forming a distinct hard-axis peak for deposition rates $\eta_{AF} \leq 1.64$ nm/min [Fig. 6(a)]. This represents an apparent biaxial anisotropy for the investigated low- η_{AF} systems not connected to the F. The amplitude of $H_{EB}(\varphi)$ is significantly suppressed for low η_{AF} .

Determined optimum parameters are shown in Fig. 7, where the dependence of $J_C^{\text{II}}(\eta_{AF})$ and $J_{EB}^{\text{III}}(\eta_{AF})$ on η_{AF} resembles $|H_{EB}(\eta_{AF})|$ and $H_C(\eta_{AF})$ presented in Fig. 5. This is not unexpected since the determined energy densities J_C^{II} and J_{EB}^{III} are proportional to the number of grains contributing to the corresponding macroscopic properties H_C and H_{EB} , respectively [4,11]. The energy density K_F connected to the FUMA shows a decreasing trend for decreasing η_{AF} , which might be caused by an inherited GVD [17] or an altered microstructure of the F CoFe layer due to the underlying AF, resulting in a strongly noncoherent F. The latter cannot be represented within the utilized model [11], where the F magnetization is assumed to coherently rotate in a uniform monodomain state during reversal. The average relaxation time τ_C^{II} of coercivity mediating grains of class II shows a clear increasing trend for deposition rates above $\eta_{AF} = 1.64$ nm/min. For $\eta_{AF} \leq 1.64$ nm/min τ_C^{II} rises [inset in Fig. 7(b)], corroborating the enhanced H_C [Fig. 5(b)] for small η_{AF} . Since τ_C^{II} depends on the mean grain size of class II grains this result also fits to the observed trend of the AF GID with η_{AF} (Fig. 3). As for low η_{AF} and high T_{FC} a melting point depression for small AF grains is assumed, and a transfer of grains from class I to class II can be connected to the significant increase of H_C and τ_C^{II} for $\eta_{AF} \leq 1.64$ nm/min and $T_{FC} = 623.15$ K. Furthermore, the comparatively large uncertainty margin for τ_C^{II} results from the spread of relaxation times of the AF grains over several orders of magnitude [11,24,47].

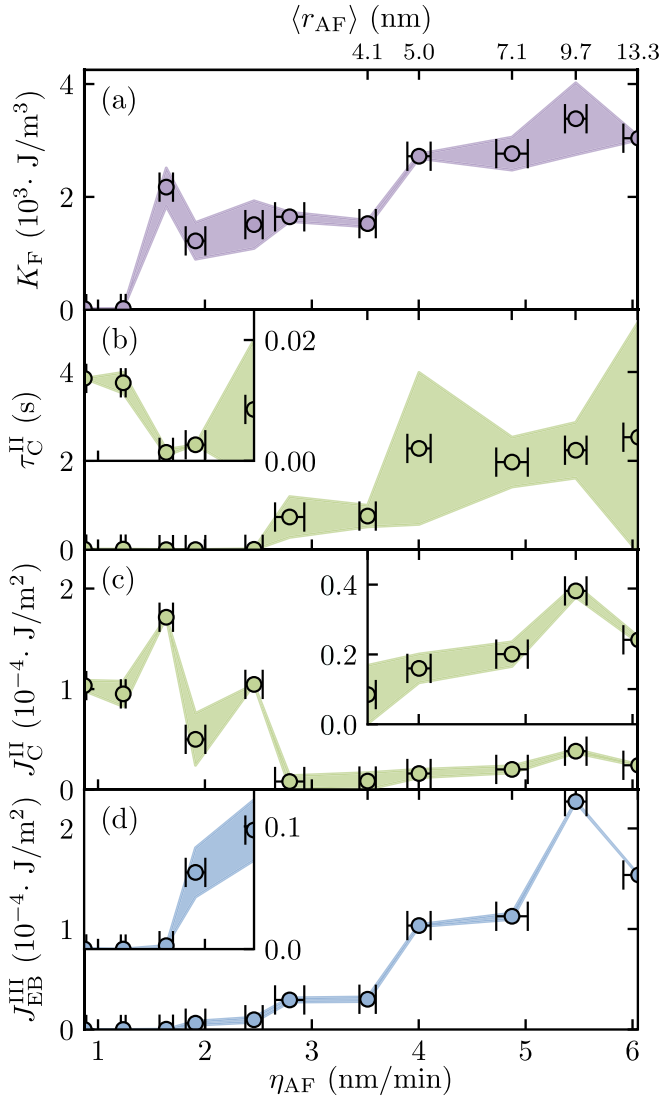


FIG. 7. η_{AF} -dependent parameters (a) K_F , (b) τ_C^{II} , (c) J_C^{II} , and (d) J_{EB}^{III} obtained from fitting model calculations to $H_C(\varphi)$ and $H_{EB}(\varphi)$. The insets have an adjusted ordinate scale for visualizing the parameter dependency for lower orders of magnitude. The upper abscissa shows the determined mean grain radii $\langle r_{AF} \rangle$ of the GID corresponding to η_{AF} .

V. CONCLUSION

We have studied the impact of the AF deposition rate on structural and magnetic properties of a prototypical polycrystalline EB layer system. The characterization of the GID and the crystal structure via AFM and XRD, respectively, allowed for the identification of a threshold deposition rate, from which the AF GID can be scaled and a homogenous crystal structure is present with a pronounced IrMn (111) orientation. The magnetic properties classifying the EB, i.e., the EB shift H_{EB} and the coercivity H_C , were investigated via angular-resolved MOKE magnetometry and can be tuned in accordance with the GID for η_{AF} above the determined threshold, which is in good agreement with the structural analysis and the utilized [11] as well as other published models for polycrystalline EB systems [4,16,47]. The influence of a field-cooling procedure was investigated via successively

increasing the temperature T_{FC} at which the process was performed. The relative increase of H_{EB} in dependence of η_{AF} and T_{FC} is correlated to the GVD as well as the independence of H_C on T_{FC} for a specific interval of η_{AF} . The distinct increase of H_C for low η_{AF} and the highest applied T_{FC} is assumed to arise from a melting point depression for small grains, which are transferred from a noncontributing grain class (class I) to class II, in which they mediate H_C and contribute to the RMA. Additionally, an extended Stoner-Wohlfarth approach was utilized, by fitting model calculations to the measured angular-resolved magnetic properties, in order to disentangle the magnetic anisotropies prevailing in polycrystalline EB systems connected to the intrinsic FUMA and the RMA as well as the UDA caused by coercivity and EB shift mediating grains of classes II and III, respectively.

The comparison of the structural and the magnetic characterization in dependence of η_{AF} and T_{FC} allowed for a correlation of macroscopic magnetic properties of polycrystalline EB systems with their microstructure as well as for the disentanglement of the individual anisotropies contributing to the magnetic characteristics. As a result, in the context of similar investigations [15,41,48,55] and common structure zone models [38–40,42], we suppose for η_{AF} above a certain threshold a polycrystalline AF layer structure with homogeneous crystallites and a columnar growth where the cross-section radius of the individual grains connected to the volume GVD equals the investigated grain radius of the analyzed GID. For lower η_{AF} an inhomogeneous layer structure is expected with random and concurring growth directions prohibiting a direct correlation between the GID and the GVD.

The evidenced impact of the AF GVD on H_{EB} and H_C verifies the model proposed in Ref. [11] and underpins its applicability, while the tight connection of the RMA to the average relaxation time τ_C^{II} of coercivity mediating grains of class II is emphasized. We have shown that by a systematic variation of η_{AF} we could connect the polycrystalline microstructure of EB bilayers with the prevailing and also time-dependent magnetic anisotropies.

ACKNOWLEDGMENT

J.Z. and K.L. acknowledge funding by the DFG (Project No. LE 2558 2-1).

APPENDIX: UNCERTAINTY OF OPTIMAL PARAMETERS

In order to determine the optimum set of fit parameters \mathbf{x}_{opt} , the sum $f^{sim}(\varphi, \mathbf{x}) = H_{EB}^{sim}(\varphi, \mathbf{x}) + H_C^{sim}(\varphi, \mathbf{x})$ is fitted to $f(\varphi) = H_{EB}(\varphi) + H_C(\varphi)$ using the *curve_fit* function from the PYTHON-based library SCIPY [66]. Ideally, this should give the same solution as for fitting the dependencies independently (triangle inequality).

The estimated covariance matrix retrieved from the used fit algorithm was almost insensitive to parameter variations; thus no meaningful uncertainty estimate for the optimum parameters could be found. To determine the quality of the optimum parameters with a set of uncertainties $\delta\mathbf{x}$, a reverse propagation of uncertainty was performed. For that reason, first the deviation of the function to be fitted, $\delta f(\varphi_i, \mathbf{x})$, depending on all measured angles φ_i , is defined via the propagation of the

deviation δx_j of the individual parameters,

$$\begin{aligned} \delta f(\varphi_i, \mathbf{x}) &= \|f^{\text{sim}}(\varphi_i, \mathbf{x}) - f(\varphi_i)\| \\ &= \sum_{x_j} \left| \frac{\partial f^{\text{sim}}(\varphi_i, \mathbf{x})}{\partial x_j} \right|_{\mathbf{x}=\mathbf{x}_{\text{opt}}} \delta x_j = \sum_{x_j} \mathcal{D}_{ij} \delta x_j, \end{aligned}$$

with \mathcal{D}_{ij} representing the gradient of the fit function in dependence of \mathbf{x} with which the individual parameter de-

viations δx_j are weighted. \mathcal{D}_{ij} is estimated with $\mathbf{x}_{\varepsilon,j} = \{x_j + \varepsilon, \{x_k \mid x_k \in \mathbf{x}_{\text{opt}} \wedge k \neq j\}\}$ via the difference quotient, where ε is chosen such that $\mathbf{x}_{\varepsilon,j}$ deviates from \mathbf{x}_{opt} by 25%. Calculations for several ε showed that the retrieved errors $\delta \mathbf{x}$ are, except for large values, not depending on ε . With $\delta f_i = \delta f(\varphi_i, \mathbf{x})$ for all angles φ_i , an overdetermined linear system of equations $\delta \mathbf{f} = \mathcal{D} \delta \mathbf{x}$ is given, which can be solved for $\delta \mathbf{x}$ via $\min_{\delta \mathbf{x}} \|\delta \mathbf{f} - \mathcal{D} \delta \mathbf{x}\|$.

-
- [1] W. H. Meiklejohn, *J. Appl. Phys.* **33**, 1328 (1962).
- [2] J. Nogués and I. K. Schuller, *J. Magn. Magn. Mater.* **192**, 203 (1999).
- [3] A. E. Berkowitz and K. Takano, *J. Magn. Magn. Mater.* **200**, 552 (1999).
- [4] K. O'Grady, L. Fernandez-Outon, and G. Vallejo-Fernandez, *J. Magn. Magn. Mater.* **322**, 883 (2010).
- [5] J. Nogués, J. Sort, V. Langlais, V. Skumryev, S. Suriñach, J. S. Muñoz, and M. D. Baró, *Phys. Rep.* **422**, 65 (2005).
- [6] W. H. Meiklejohn and C. P. Bean, *Phys. Rev.* **105**, 904 (1957).
- [7] C. Binns, M. T. Qureshi, D. Peddis, S. H. Baker, P. B. Howes, A. Boatwright, and S. C. Cavill, *Nano Lett.* **13**, 3334 (2013).
- [8] M. Phan, J. Alonso, H. Khurshid, P. Lampen-Kelley, S. Chandra, K. S. Repa, Z. Nemati, R. Das, Ó. Iglesias, and H. Srikanth, *Nanomaterials* **6**, 221 (2016).
- [9] B. Kuerbanjiang, U. Wiedwald, F. Haering, J. Biskupek, U. Kaiser, P. Ziemann, and U. Herr, *Nanotechnology* **24**, 455702 (2013).
- [10] F. Radu and H. Zabel, *Magnetic Heterostructures* (Springer, New York, 2008), p. 97.
- [11] N. D. Müglic, A. Gaul, M. Meyl, A. Ehresmann, G. Götz, G. Reiss, and T. Kuschel, *Phys. Rev. B* **94**, 184407 (2016).
- [12] L. Alonso, T. R. F. Peixoto, and D. R. Cornejo, *J. Phys. D: Appl. Phys.* **43**, 465001 (2010).
- [13] F. Radu, A. Westphalen, K. Theis-Bröhl, and H. Zabel, *J. Phys.: Condens. Matter* **18**, L29 (2005).
- [14] J. Geshev, L. G. Pereira, and J. E. Schmidt, *Phys. Rev. B* **66**, 134432 (2002).
- [15] M. Vopsaroiu, G. V. Fernandez, M. J. Thwaites, J. Anguita, P. J. Grundy, and K. O'Grady, *J. Phys. D* **38**, 490 (2005).
- [16] A. Harres and J. Geshev, *J. Phys.: Condens. Matter* **24**, 326004 (2012).
- [17] M. Vopsaroiu, M. Georgieva, P. J. Grundy, G. V. Fernandez, S. Manzoor, M. J. Thwaites, and K. O'Grady, *J. Appl. Phys.* **97**, 10N303 (2005).
- [18] N. P. Aley, G. Vallejo-Fernandez, R. Kroeger, B. Lafferty, J. Agnew, Y. Lu, and K. O'Grady, *IEEE Trans. Magn.* **44**, 2820 (2008).
- [19] A. Kohn, A. Kovács, R. Fan, G. J. McIntyre, R. C. C. Ward, and J. P. Goff, *Sci. Rep.* **3**, 2412 (2013).
- [20] A. P. Malozemoff, *Phys. Rev. B* **35**, 3679 (1987).
- [21] A. Ehresmann, D. Junk, D. Engel, A. Paetzold, and K. Röhl, *J. Phys. D* **38**, 801 (2005).
- [22] A. Gaul, S. Hankemeier, D. Holzinger, N. D. Müglic, P. Staack, R. Frömter, H. P. Oepen, and A. Ehresmann, *J. Appl. Phys.* **120**, 033902 (2016).
- [23] A. Gaul, D. Emmrich, T. Ueltzhöffer, H. Huckfeldt, H. Doganay, J. Hackl, M. I. Khan, D. M. Gottlob, G. Hartmann, and A. Beyer, *Beilstein J. Nanotechnol.* **9**, 2968 (2018).
- [24] N. D. Müglic, M. Merkel, A. Gaul, M. Meyl, G. Götz, G. Reiss, T. Kuschel, and A. Ehresmann, *New J. Phys.* **20**, 053018 (2018).
- [25] Y. Zhang, X. Ruan, B. Liu, Z. Xu, Q. Xu, J. Shen, Q. Li, J. Wang, B. You, and H. Tu, *Appl. Surf. Sci.* **367**, 418 (2016).
- [26] I. Berthold, U. Löschner, J. Schille, R. Ebert, and H. Exner, *Phys. Procedia* **56**, 1136 (2014).
- [27] E. Albisetti, D. Petti, M. Pancaldi, M. Madami, S. Tacchi, J. Curtis, W. P. King, A. Papp, G. Csaba, and W. Porod, *Nat. Nanotechnol.* **11**, 545 (2016).
- [28] D. Holzinger, N. Zingsem, I. Koch, A. Gaul, M. Fohler, C. Schmidt, and A. Ehresmann, *J. Appl. Phys.* **114**, 013908 (2013).
- [29] J. Zehner, R. Huhnstock, S. Oswald, U. Wolff, I. Soldatov, A. Ehresmann, K. Nielsch, D. Holzinger, and K. Leistner, *Adv. Electron. Mater.* **5**, 1900296 (2019).
- [30] A. Ehresmann, I. Koch, and D. Holzinger, *Sensors* **15**, 28854 (2015).
- [31] D. Holzinger, I. Koch, S. Burgard, and A. Ehresmann, *ACS Nano* **9**, 7323 (2015).
- [32] E. C. Stoner and E. P. Wohlfarth, *Nature* **160**, 650 (1947).
- [33] E. C. Stoner and E. P. Wohlfarth, *Philos. Trans. R. Soc.* **240**, 599 (1948).
- [34] M. D. Stiles and R. D. McMichael, *Phys. Rev. B* **59**, 3722 (1999).
- [35] J. Saha and R. H. Victora, *Phys. Rev. B* **73**, 104433 (2006).
- [36] A. Ajan and I. Okamoto, *J. Appl. Phys.* **92**, 6099 (2002).
- [37] D. E. Laughlin, B. Cheong, Y. C. Feng, D. N. Lambeth, and L. L. Lee, *Scr. Metall. Mater.* **33**, 1525 (1995).
- [38] J. A. Thornton, *J. Vac. Sci. Technol.* **11**, 666 (1974).
- [39] J. A. Thornton, *J. Vac. Sci. Technol.* **12**, 830 (1975).
- [40] P. Barna and M. Adamik, *Thin Solid Films* **317**, 27 (1998).
- [41] M. Vopsaroiu, M. J. Thwaites, G. V. Fernandez, S. Lepadatu, and K. O'Grady, *J. Opt. Adv. Mater.* **7**, 2713 (2005).
- [42] C. V. Thompson, *Annu. Rev. Mater. Sci.* **30**, 159 (2000).
- [43] J. B. Sousa, J. A. M. Santos, R. F. A. Silva, J. M. Teixeira, J. Ventura, J. P. Araújo, P. P. Freitas, S. Cardoso, and Y. G. Pogorelov, *J. Appl. Phys.* **96**, 3861 (2004).
- [44] S. J. Gamble, M. H. Burkhardt, A. Kashuba, R. Allenspach, S. S. P. Parkin, H. C. Siegmman, and J. Stöhr, *Phys. Rev. Lett.* **102**, 217201 (2009).
- [45] D. Necas, *Cent. Eur. J. Phys.* **10**, 181 (2012).
- [46] S. Nieber and H. Kronmüller, *Phys. Status Solidi B* **165**, 503 (1991).

- [47] E. Fulcomer and S. H. Charap, *J. Appl. Phys.* **43**, 4190 (1972).
- [48] G. Vallejo-Fernandez, N. P. Aley, J. N. Chapman, and K. O'Grady, *Appl. Phys. Lett.* **97**, 222505 (2010).
- [49] G. Vallejo-Fernandez, L. E. Fernandez-Outon, and K. O'Grady, *Appl. Phys. Lett.* **91**, 212503 (2007).
- [50] S. Gates-Rector, *Powder Diffr.* **34**, 352 (2019).
- [51] M. Wojcik, J. P. Jay, P. Panissod, E. Jedryka, J. Dekoster, and G. Langouche, *Z. Phys. B* **103**, 5 (1997).
- [52] B. D. Cullity, *Elements of X-Ray Diffraction* (Addison-Wesley, Reading, MA, 1978).
- [53] M. Birkholz, *Thin Film Analysis by X-Ray Scattering* (Wiley-VCH, Weinheim, 2006).
- [54] J. I. Langford and D. Louër, *J. Appl. Crystallogr.* **15**, 20 (1982).
- [55] J. H. Hsu, A. C. Sun, and P. Sharma, *Thin Solid Films* **542**, 87 (2013).
- [56] P. Buffat and J. P. Borel, *Phys. Rev. A* **13**, 2287 (1976).
- [57] S. L. Lai, J. Y. Guo, V. Petrova, G. Ramanath, and L. H. Allen, *Phys. Rev. Lett.* **77**, 99 (1996).
- [58] D. R. Lide and W. M. Haynes, *CRC Handbook of Chemistry and Physics*, 90th ed. (CRC Press, Boca Raton, FL, 2010).
- [59] H. J. Bargel and G. Schulze, *Werkstoffkunde* (Springer, Berlin, 2012).
- [60] A. Safaei, M. Attarian Shandiz, S. Sanjabi, and Z. H. Barber, *J. Phys. Chem. C* **112**, 99 (2008).
- [61] P. Antoniammal and D. Arivuoli, *J. Nanomater.* **2012**, 415797 (2012).
- [62] E. Jimenez, J. Camarero, J. Sort, J. Nogues, A. Hoffmann, F. J. Teran, P. Perna, J. M. Garcia-Martin, B. Dieny, and R. Miranda, *Appl. Phys. Lett.* **95**, 122508 (2009).
- [63] E. Jimenez, J. Camarero, P. Perna, N. Mikuszeit, F. J. Teran, J. Sort, J. Nogues, J. M. Garcia-Martin, A. Hoffmann, B. Dieny, and R. Miranda, *J. Appl. Phys.* **109**, 07D730 (2011).
- [64] E. Jimenez, J. Camarero, J. Sort, J. Nogues, N. Mikuszeit, J. M. Garcia-Martin, A. Hoffmann, B. Dieny, and R. Miranda, *Phys. Rev. B* **80**, 014415 (2009).
- [65] H. Huckfeldt, A. Gaul, N. David Möglich, D. Holzinger, D. Nissen, M. Albrecht, D. Emmrich, A. Beyer, A. Götzhauser, and A. Ehresmann, *J. Phys.: Condens. Matter* **29**, 125801 (2017).
- [66] P. Virtanen, R. Gommers, T. E. Oliphant, M. Haberland, T. Reddy, D. Cournapeau, E. Burovski, P. Peterson, and W. Weckesser, *Nat. Methods* **17**, 261 (2020).